Selective Uptake Into Drug Resistant Mammalian Cancer by Cell Penetrating Peptide-Mediated Delivery

Kate J. F. Carnevale,[†] Megan E. Muroski,[†,§] Parth N. Vakil,[†] Megan E. Foley,[†,‖] Geoffry Laufersky,[†,⊥] Rachael Kenworthy,[†,#] Diego A. R. Zorio,[‡] Thomas J. Morgan, Jr.,[‡] Cathy W. Levenson,[‡] and Geoffrey F. Strouse*,[†]

[†]Dept. of Chemistry and Biochemistry, Florida State University, Tallahassee, Florida 32304, United States
[‡]College of Medicine, Florida State University, Tallahassee, Florida 32304, United States

S *Supporting Information*

ABSTRACT: Research over the past decade has identified several of the key limiting features of multidrug resistance (MDR) in cancer therapy applications, such as evolving glycoprotein receptors at the surface of the cell that limit therapeutic uptake, metabolic changes that lead to protection from multidrug resistant mediators which enhance degradation or efflux of therapeutics, and difficulty ensuring retention of intact and functional drugs once endocytosed. Nanoparticles have been demonstrated to be effective delivery vehicles for a plethora of therapeutic agents, and in the case of nucleic acid based agents, they provide protective advantages. Functionalizing cell penetrating peptides, also known as protein transduction domains, onto the surface of fluorescent quantum dots creates a

labeled delivery package to investigate the nuances and difficulties of drug transport in MDR cancer cells for potential future clinical applications of diverse nanoparticle-based therapeutic delivery strategies. In this study, eight distinct cell penetrating peptides were used (CAAKA, HSV1-VP22, HIV-TAT, HIV-gp41, Ku-70, hCT(9-32), integrin-β3, and K-FGF) to examine the different cellular uptake profiles in cancer versus drug resistant melanoma (A375 & A375-R), mesothelioma (MSTO & MSTO-R), and glioma (rat 9L and 9L-R, and human U87 & LN18) cell lines. The results of this study demonstrate that cell penetrating peptide uptake varies with drug resistance status and cell type, likely due to changes in cell surface markers. This study provides insight into developing functional nanoplatform delivery systems in drug resistant cancer models.
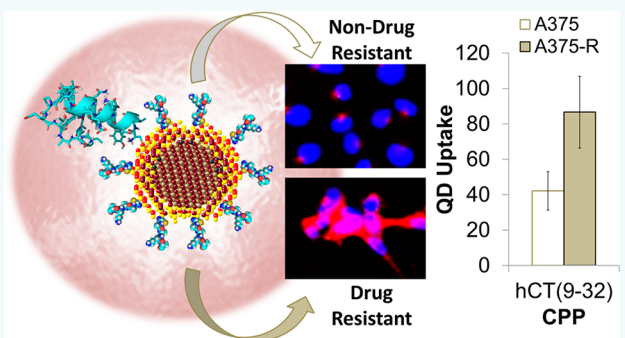
INTRODUCTION

Nonviral approaches to overcoming drug resistant pathways include the use of cell penetrating peptides (CPPs) coupled to nanoparticles to effectively act as a transfection carrier of chemotherapeutics.[1] CPPs are derived from small sequence fragments of the protein transduction domain of viral sheath proteins or human carrier proteins. Packaging of CPPs onto the surface of nanoparticles is an important focus area for packaging of therapeutics into nonviral transfection methodologies.[2−5] When the nanoparticle—loaded with a therapeutic agent—is combined with a CPP, cellular uptake and delivery of the therapeutic agent can be enhanced. Nanotherapeutic delivery agents have also been shown to enhance the survivability and therefore effectiveness of the delivered nucleic acid agent due to reduced nuclease activity, continuous agent release, and pH clamping of the endosomal package.[6,7]

There are reports suggesting that CPPs exhibit selectivity for different cell types.[8−13] Thus, we have hypothesized that CPPs may also exhibit specificity for chemoresistance in different cancer cells and have designed an approach to screen CPPs for nanocarrier uptake of multishelled CdTe@CdSe@CdS@ZnS

quantum dots (QDs) (Figure 1) and investigate the effective enhancement of cellular internalization in a series of cancer cell lines of human melanoma (A375), human mesothelioma (MSTO), and human (LN18, U87) and rat glioma (9L), along with drug resistant subclones. QDs are used for this study as they are ideal optical probes for molecular tracking in cell uptake studies owing to their brightness and resistance to photobleaching, and for their comparability to other clinically relevant, nonemissive, nanomaterials. Although the heavy metals that comprise QDs and allow for the unique optical properties -- such as cadmium and tellurium -- are potentially cytotoxic and therefore not applicable to potential clinical treatments, the use of a non-therapeutic photoluminescent multishelled QD (composed of CdTe@CdSe@CdS@ZnS), allows for quantification of nanopackage cellular uptake through fluorescence microscopy and provides clinically transferrable insights. The studied CPPs are appended to the

A

hCT (9-32)

CAAKA

B
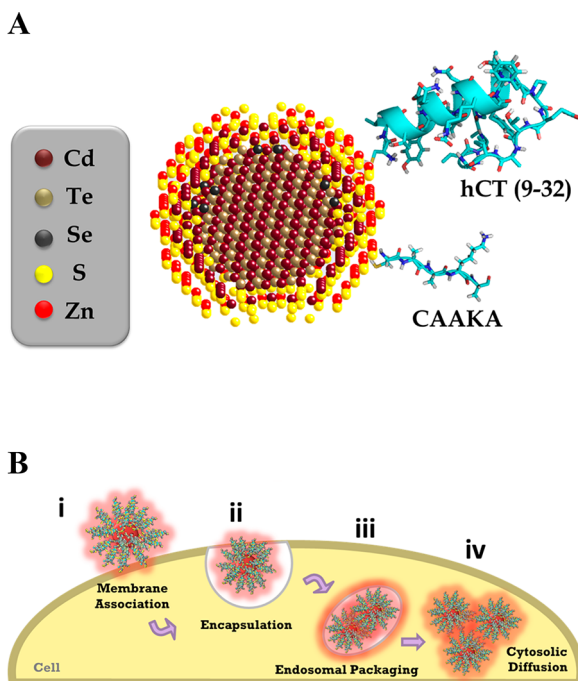
Figure 1. (A) Schematic diagram of CdTe@CdSe@CdS@ZnS multishelled QD showing peptide functionalization with CAAKA and hCT(9-32). (B) Graphic of QD-CPP cellular uptake, showing cellular membrane association (i), internalization (ii), and endosomal entrapment (iii) versus cytosolic distribution (iv).

QD surface via an N-terminal cysteine which allows for bidentate coordination using the thiol and amine of cysteine to bind onto the outermost ZnS layer of the QD shell. A biphasic ligand exchange allows the displacement of the weakly coordinated organic passivating ligands from the as-synthesized QDs and replacement by the aqueous CPPs.

The study provides a method that shows promise for selectively targeting multidrug resistant cancers and could pave the way for new therapies that increase drug delivery into tumors, while circumventing drug efflux and other mechanisms responsible for chemoresistance. Despite improvements in therapeutic approaches for many types of cancer, the development of multidrug resistance (MDR) remains a significant barrier to improving survival time in patients with many types of aggressive cancers. Developing new potentially therapeutic strategies for highly aggressive, metastatic cancers with poor 5-year survival rates (melanoma (<20%), meso-thelioma (<5%), and gliosarcoma (<10%)) is important.[14−21]

The results of the study could be translated to clinically applicable nonviral delivery vectors such as polymer nano-particles, nanooxides, nanometals, or other nanocarriers.

■ RESULTS AND DISCUSSION

The ability of CPP-labeled nanoparticles to utilize endocytotic pathways and bypass multidrug resistance efflux pumps makes them an attractive choice for drug delivery.[9,10,22,23] Figure 1 shows a schematic of the CPP labeled multishelled QD used to assess the cellular uptake dependence for drug resistant cells relative to drug naive cells. The selected protein derived cell penetrating peptide sequences (Table 1) were selected from the literature and modified to have a cysteine residue at the N-terminus for functional attachment to the ZnS surface of the multishelled QD and to allow for biphasic ligand exchange of the as-synthesized organic capping ligands, to provide aqueous solubility. As shown previously, the cysteine strongly coordinates to the surface through a metal−ligand bond.[24] The multishelled QDs used for the study were prepared by modified literature protocols for stepwise SILAR shelling methods.[25] Detailed characterization of the QD can be found in the Supporting Information, including TEM, size distribu-tion, absorbance, and emission profiles for the core of CdTeSe, the CdS shell, and the final ZnS shell (Supporting Information Figure SF1).

The general cellular uptake mechanism of CPPs is highly debated and appears to be sequence and cell-surface specific, with no verified predictability established in the literature.[8,26,27] The CPPs in Table 1 were chosen to explore the uptake behavior and selectivity for drug resistant versus chemo-therapeutic sensitive cancer cell lines for highly charged peptides using HSV1-VP22 (+6) and HIV-TAT (+9), compared to the low and neutral charges found in the CPP sequence for hCT(9-32) (+1), K-FGF (+1), Ku70 (+0), integrin ß3 (+0), and HIV-gp41 (+0).

The CPPs are coloaded onto the QD surface at a 9:1 ratio with a short synthetic peptide sequence, CAAKA, which acts as a space-filling peptide to better passivate the QD surface while maintaining loose packing of the target CPP sequences, due to the shorter sequence length, and alternating hydrophobic and hydrophilic characteristics of CAAKA versus the other CPPs of Table 1.

The looser packing acheived by coloading also allows the target CPP sequence to have more visibility to the cell, allowing for better sequence recognition at the cell surface, as well as reducing the overall surface charge that leads to insolubility with the highly charged peptides.[28] Three of the

Table 1. Table of Selected Cell Penetrating Peptides, Displaying Numerical Designation, CPP Name, Sequence and Length, Charge and Isoelectric Point (P$_i$) at pH 7.4, Molecular Weight in Daltons, and Percentage of Hydrophobic Residues (L%)[a]

CPP	Sequence & Origin	Length	Charge at pH 7.4	Pi	MW, Da	L%
CAAKA	CAAKA ⊥	5	+1	8.97	462.60	75
HSV1-VP22	C*DAATATRGRSAASRPTERPRAPARSASRPRRPVD †	35	+6	12.3	3748.17	40
HIV-TAT	C*YGRKKRRQRRR †	12	+8	12.4	1663.00	0
HIV-gp41	C*GALFLGWLGAAGSTMGA †	18	+0	5.33	1682.99	56
Ku-70	C*PMLKE ‡	6	+0	6.28	719.90	60
hCT(9-32)	C*LGTYTQDFNKFHTFPQTAIGVGAP ‡	25	+1	7.1	2714.08	40
integrin ß3	C*VTVLALGALAGVGVG ‡	16	+0	5.33	1399.71	63
K-FGF	C*AAVALLPAVLLAHLLAP ‡	18	+1	7.15	4533.06	94

[a]CPP origin is denoted by ⊥ for synthetic, † for viral proteins, and ‡ for nonviral proteins. * denotes cysteine mutation, not present in the original sequence.

selected peptides in Table 1, HSV1-VP22, HIV-TAT, and HIV-gp41 (Table 1), are derived from segments of viral proteins that have an added cysteine mutation at the N-terminus. HSV1-VP22 is a truncation of the tegument protein, viral protein 22 (VP22) found in herpes simplex virus (HSV-1).[29−32] HIV-TAT and HIV-gp41 are derived from subunits of viral capsid proteins of the human immunodeficiency virus type-1 (HIV-1). HIV-TAT is a fragment of the transactivator of transcription (TAT) protein, and HIV-gp41 is derived from the HIV glycoprotein 41 (gp-41).[32,33] These three viral peptides have successfully been utilized to transport cargo across the cell membrane in various cell lines.[30−38] Although the exact mechanism of internalization for these viral CPPs is still contested, it is thought that the peptides enter through one of the mechanisms of endocytosis.[39] The remaining CPPs are cysteine modified peptide fragments from proteins identified from the literature, known to induce cellular uptake. Ku-70 is derived from the Bax-binding domain of the protein Ku-70, which acts in DNA repair inside the nucleus.[40] The excised Ku-70 peptide sequence is also known as a Bax-inhibiting peptide (Bip) and has demonstrated low toxicity in cells, but the internalization mechanism is also undetermined.[41] hCT(9-32) is derived from the C-terminal fragment of the human calcitonin protein hormone and is also thought to internalize through a mechanism of endocytosis; however, it is suggested that high concentrations are needed to facilitate membrane disruption.[42−44] The CPPs integrin β3 and K-FGF are both derived from fragments of signal sequences of proteins. The integrin β3 peptide sequence originates from the hydrophobic region of the signal sequence of human integrin β3 protein.[45] Similarly, the K-FGF peptide sequence originates from the signal sequences of fibroblast growth factor found in Kaposi's sarcoma cells.[46,47] Integrin β3 and K-FGF peptide sequences have been observed to enter cells by means of endocytosis, but it is believed that direct translocation across the membrane may also be possible for such highly hydrophobic molecules.[48−51]

The CPPs are exchanged onto the QD surface by displacement of the initial trioctylphosphine (TOP) passivation layer on the organically soluble multishelled QD using a biphasic exchange process (Figure 2). The selected CPPs were coupled to the QD surface at a loading ratio of 9:1 CAAKA to CPP-X. CAAKA is used as a synthetic spacer peptide to allow for the longer CPPs to avoid tightly packing on the QD surface, as this may hinder sequence recognition by the target cells. A molar excess of 1000:1 peptide to QD was used to drive the aqueous transfer of the previously organically soluble QDs. The peptide loading levels for the studied CPPs are believed to be the same within statistical error, although direct quantitative confirmation of the CPP ratio loading levels on the QDs was not directly measured. Although the presence of peptides was detected in NMR, IR, and MS (data not shown), attempts to quantitatively extract the CPP loading levels led to nonquantitative results due to low material quantities and difficulty in ensuring complete CPP cleavage from the QD surface. Additionally, differences in ionizability of the peptides were found to hinder quantification of peptide concentrations by ESI-MS, providing nonlinear calibration curves of concentration to signal intensity (data not shown).

In a typical biphasic exchange, the QD, dissolved in trichloroethylene (TCE), was observed to transfer to the upper aqueous, peptide-containing layer within 1 h. By increasing the alkalinity of the aqueous phase (pH > 8.0,
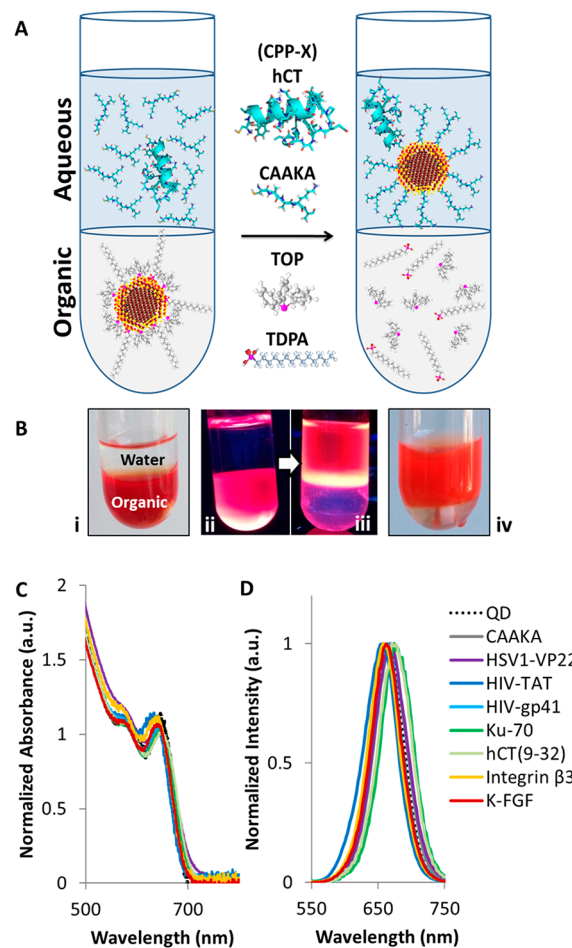
Figure 2. Passivation of the CdTe@CdSe@CdS@ZnS multishelled QDs biofunctionalized with cell penetrating peptides CAAKA, HSV1-VP22, HIV-TAT, HIV-gp41, Ku-70, hCT(9-32), integrin β3, and K-FGF. Schematic (A) depicts exchange of organic ligands, TOP and TDPA, for 10% CPP-X and 90% CAAKA. Image (B) displays QD solution before and after phase exchange in room light (i and iv) and under UV excitation (ii and iii). The absorbance (C) and emission (D) spectra for each QD-peptide sample show slight changes in the surface environment per peptide.

NH$_2$-terminus p$K_a \sim 8$), the peptide is deprotonated and transports the QD from the organic to the aqueous layer. Neutralization of the aqueous layer and back extraction yielded water-soluble QDs, capable of use in the biological application. As shown in Figure 2, the exchange of the peptide onto the QD surface is evidenced by aqueous solubility and a shift in the absorption and emission properties. The absorbance and emission spectral profiles of the QD-CPPs are observed to shift slightly with the changing molecular environment at the surface of the QD due to the unique chemical properties of the loaded CPPs (Figure 2C and D). Relatedly, the quantum yields (Φ) for the aqueous QDs are dependent on the identity of the peptide coating as well. The experimental data are tabulated in Table 2. The spectral window and quantum yields are accounted for in the cell studies to allow for more accurate quantification of cellular uptake.

The isolated QD-CPPs show a shift of the absorption maximum following CPP exchange which can reflect the dielectric of the solvent and peptide or changes in particle size. The size of the QD-CPPs were measured by TEM (Table 2 and Supporting Information Figure SF2), for five of the eight

Table 2. Characterization of CPP Functionalized QDs, Showing CPP-Dependent Quantum Yield (Φ), First Exciton Absorption Wavelength (λ_{Abs}), and Maximum Photoluminescence Wavelength (λ_{PL}), TEM Diameter (d), Zeta Potential (ζ), and Mobility (m) in 0.7% Agarose Gel[a]

| QD-CPP	Φ (%)	λ_{Abs} (nm)	λ_{PL} (nm)	d (nm)	ζ (mV)	m (cm)
CAAKA	11.3	644	670	4.0 ± 0.8	-34.7 ± 0.6	2.6
HSV1-VP22	7.4	644	668	3.9 ± 0.4	$+14.0 \pm 0.9$	2.4
HIV-TAT	37.0	632	658	4.0 ± 0.3	-36.2 ± 1.9	2.4
HIV-gp41	8.3	643	664	--	$+14.0 \pm 0.3$	2.3
Ku-70	2.3	644	674	4.0 ± 0.3	-2.3 ± 0.5	2.6
hCT(9-32)	2.4	648	670	4.1 ± 0.3	-2.7 ± 3.0	2.3
integrin ß3	18.4	643	658	--	$+16.4 \pm 1.5$	2.3
K-FGF	12.4	639	664	--	-27.3 ± 2.2	2.8

[a]-- indicates values not measured.

samples CPP functionalizations, and were observed to be consistent with the materials prior to CPP surface modification (due to the availability of instrumentation time and cost, the three remaining samples were assumed to maintain the same particle size). This indicates the absorption changes are due to the dielectric function attributed to the different peptide functionalizations and not changes to the QD-CPP size. The results are consistent with the experimental observation that electrophoresis mobility in a 0.7% agarose gel is nearly identical (Supporting Information Figure SF3). The mobility differences can be influenced by both size and charge. In the electrophoretic gel experiment it is observed that all the QD-CPPs move toward the cathode in the electrophoretic gel indicating negative surface charge. Analysis of the zeta potentials for the QD-CPPs confirms the QD-CPPs are primarily negatively charged, although close to zero (Table 2). The result is surprising as all the peptides should be neutral at the pH of the study. For comparison, a negatively charged nonpeptide ligand, dihydrolipoic acid (DHLA), exhibits a zeta potential of -16 mV, consistent with earlier DHLA-QD reports.[52] The results suggest that the observed zeta potentials for the QD-CPPs are more complex than total CPP charge. The observed potentials are influenced by facet expression, ligand packing, screening of charge near the nanoparticle surface, and folding orientation of the CPPs on the QD surface. The observed shift in absorption for the peptides implies changes in the dielectric function, and this can be a result of charge screening effects. Further studies are underway to understand the correlations; however, the observation is important as it implies the experimental observables for classical biological methods are strongly influenced by the materials. Additionally, the isolated samples are stable in DI water for >3 years. While others have reported that zeta potentials closer to zero than ± 30 mV are indicative of noncolloidally stable nanomaterials,[53] this is not observed in these studies.

Cellular Uptake Studies. The QD-CPP constructs were used to challenge the drug resistant and naive cancer cell lines for a 24 h incubation period, and the cells were then washed with PBS, fixed, and colabeled with DAPI nuclear stain, as described in the Experimental Section. Fixed cells were imaged using a wide field inverted fluorescence microscope for each QD-CPP treatment (Figure 3). Figure 3 displays fluorescence images of the blue DAPI nuclear stain and red intracellular QD emission as well as overlays with the differential interference contrast (DIC) bright field channel to visualize cellular boundaries and morphology. All cell lines appear healthy at the time of fixation, indicating no toxic effect from the 24 h

QD incubation. Red photoluminescence of the QDs within each cell line was visible at varying intensities, depending on the peptide functionalization and cell line, indicative of differential cellular uptake and processing of the QDs being correlated with the identity of the covalently attached CPP. In addition to uptake differences being peptide specific, individual cell types presented unique QD-CPP fluorescence profiles. This may potentially indicate an effect from differential phenotypic expression of cell membrane surface components between various tissue types and drug resistance status on the interactions of the CPPs, leading to increased or decreased cellular internalization of the QD-CPP agents. Additionally, the morphological patterns of intracellular QD photoluminescence were observed for each QD-CPP per cell line (Figure 3). Small punctate patterns are indicative of endosomal encapsulation of the QD-CPP construct, whereas the observation of diffuse, evenly distributed intensity throughout the cell represents cytosolic localization of the QD-CPP agents. To quantify QD-CPP cellular uptake and localization in endosomes versus cytosol, the intensity levels of red photoluminescence within the cells were analyzed using Nikon Elements and ImageJ Software. Images were background subtracted and normalized to maximum intensity per cell number, and the extracted fluorescence values were corrected for relative differences in quantum efficiency for each QD-CPP construct, to allow for accurate comparison of cellular uptake. In Figure 4, the corrected cellular uptake of each QD-CPP construct is displayed in comparison to naive and resistant cell lines, for melanoma skin cancer (Figure 4A), mesothelioma lung cancer (Figure 4B), and rat gliosarcoma brain cancer (Figure 4C), as well as for both human patient excised MDR glioblastoma cell lines (Figure 4D). Uptake profiles plotted from analysis of the QD intensity in the microscopy data reveals cellular uptake selectivity for the CPPs that are cell line specific. HSV1-VP22, Ku-70, and hCT(9-32) exhibit preferential cellular uptake in the drug resistant A375-R line versus the naive A375 line, with a statistical significance of $p \leq 0.05$ for HSV1-VP22 and hCT(9-32) and $p \leq 0.01$ for Ku-70 (Figure 4A). A similar trend was observed for hCT(9-32) and HIV-gp41 in the 9L rat gliosarcoma drug resistant line versus the drug naive cells, with a statistical significance of $p \leq 0.0001$ and $p \leq 0.01$, respectively (Figure 4C). And although no direct comparison with drug naive human glioblastoma cells was able to be obtained for this study, both human MDR glioblastoma cell lines displayed the highest uptake for Ku-70 and hCT(9-32) (Figure 4D). Interestingly, contrasting results were observed for the mesothelioma cell lines where the naive MSTO cell lines showed the opposite trend in uptake compared to the
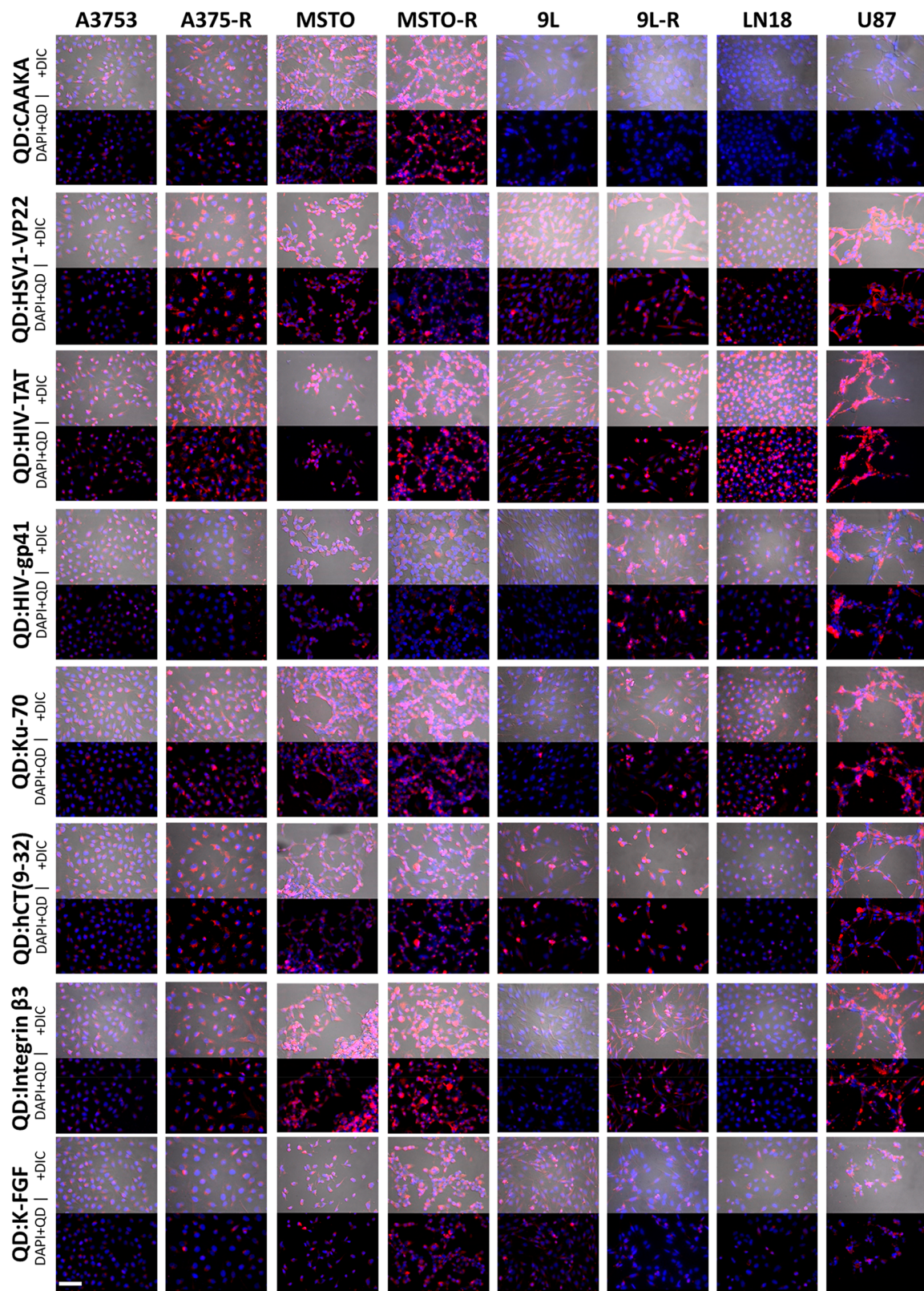
Figure 3. Fluorescence microscopy images showing red fluorescence from QD-CPP uptake in human melanoma (A375) and drug resistant (A375-R), human mesothelioma (MSTO) and drug resistant (MSTO-R), rat gliosarcoma (9L) and drug resistant (9L-R), and human patient drug resistant glioblastoma (LN18 & U87), fixed at 24 h post-transfection, with blue DAPI nuclear stain. Bright field differential interference contrast (DIC) overlay images are also shown to visualize cellular morphologies. Scale bar is 100 μm.

drug resistant line, and experienced higher QD-CPP uptake of Ku-70 and hCT(9-32), versus the drug resistant line (Figure 4B), highlighting the complexity of the CPP-cell surface interaction. Further studies are underway to understand the nature of the cell−CPP interactions leading to the observed results.
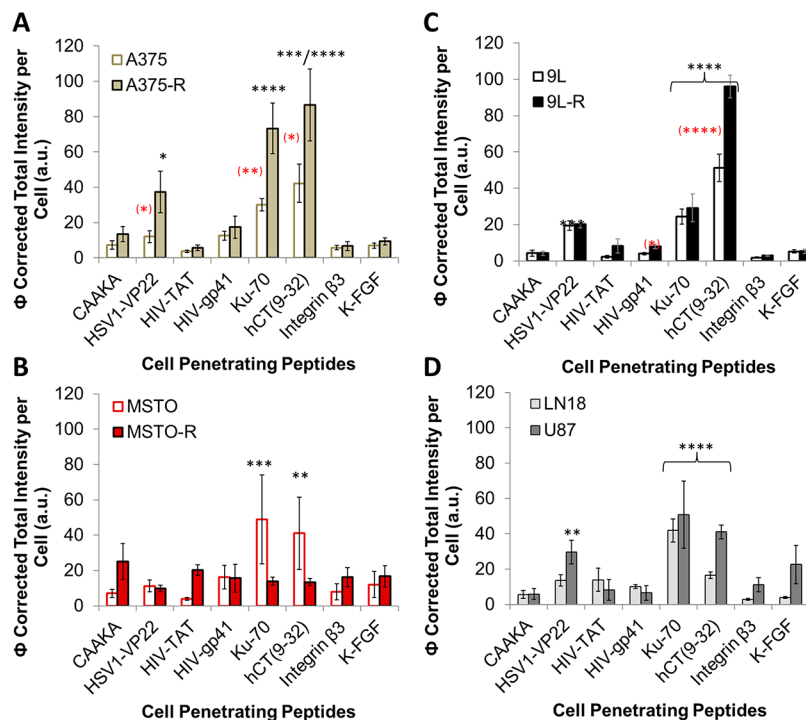
Figure 4. Uptake profiles of the studied QD-CPP constructs in (A) human melanoma (A375) and drug resistant (A375-R), (B) human mesothelioma (MSTO) and drug resistant (MSTO-R), (C) rat gliosarcoma (9L) and drug resistant (9L-R), and (D) human patient drug resistant glioblastoma (LN18 & U87), fixed at 24 h, measured by microscopic fluorescence intensity, corrected for the quantum yield of each peptide-QD conjugate, and normalized for cell number by DAPI nuclear stain counting. Displaying statistical differences of $p \le 0.5$, 0.1, 0.001, and 0.0001 as *, **, ***, and ****, respectively, for uptake in comparison to 100% CAAKA loaded QDs (black), and drug resistant versus drug naive cell lines (red, in parentheses).

Since the QDs were loaded with CPPs at a ratio of 9:1 with the CAAKA short synthetic peptide spacer, occupying 90% of the QD surface sites, to allow for better visibility of the literature-sourced sequences in Table 1 to be accessible by the cell surface, analysis of QD-CPP cellular uptake versus the 100% CAAKA loaded QD was performed as a control. It was found that, for all cell lines, QDs with 10% loading with Ku-70 and hCT(9-32) showed improved uptake versus CAAKA alone, giving the statistical significance of $p \le 0.0001$ for all lines except for A375 (hCT(9-32) $p \le 0.001$), MSTO (Ku-70 $p \le 0.001$ and hCT(9-32) $p \le 0.01$), and MSTO-R, the latter of which did not show statistical significance above the 100% CAAKA-QD sample for any of the tested constructs (Figure 4). Additionally, the Herpes virus derived peptide, HSV1-VP22, showed significant uptake over the 100% CAAKA loaded QDs in 9L and 9L-R ($p \le 0.001$), U87 ($p \le 0.01$), and A375-R ($p \le 0.5$) (Figure 4). Together, the QD-CPP uptake results demonstrate statistically significant impact from both the CPP sequence as well as the cell type. These data emphasize the complex and somewhat ambiguous nature of CPP cellular targeting and stress the need for a more comprehensive understanding of design considerations for cell-specific CPP targeting approaches to be fully realized.

Cellular Localization Analysis. The CPP modified QDs were analyzed for intracellular particle localization, to probe the question of whether an endosomal versus cytosolic fate for the QD-CPPs is a cell- or CPP-dependent phenomenon. In Figure 5A, high resolution confocal z-stack images display cellular localization of internalized QD-CPPs in three-dimensional space, with an example of more endosomal punctate fluorescence shown for the 100% CAAKA loaded QD control

(Figure 5A-i), and more cytosolic diffuse localization for 10% hCT(9-32) loaded QDs (Figure 5A-ii), at 24 h post transfection with the QD-CPP constructs. From these and previous cell images, it can be seen that all of the QD-CPP constructs display varying proportions of both punctate and diffuse fluorescence indicating different packing and escape profiles for each cell line that do not seem to be entirely CPP-dependent (Figures 5A and 3). In order to assess cytosolic versus endosomal localization of the QD-CPP packages within cells, two-dimensional cell images were analyzed for the average fluorescence area, with small punctate fluorescence areas indicating endosomal localization and large diffuse fluorescence areas indicating cytosolic QD-CPP distribution (Figure 5B). Comparing the results of Figure 5B to the average 2D area of a whole cell (~900 μm^2) versus that of a single endosome (~10 μm^2), it is observed that most of the internalized QD-CPPs were at least partially confined to endosomes with some QD-CPPs having been cytosolically delivered or having begun to diffuse into the cytosol by the 24 h time point, as the average package size for all CPPs and cell types is well below the "whole cell" or fully cytosolic value of 900 μm^2. Taking a closer look at the average fluorescence package sizes of QD-CAAKA versus the best uptake performers, HSV1-VP22, Ku-70, and hCT(9-32), it can be seen that the localization profiles seem to be predominantly cell-type dependent (Figure 5Bii-iv). The A375 and A375-R skin cancer cells show greater than 10 μm^2 average package sizes for all peptides, although package sizes of 20−30 μm^2 could be indicative of small endosomal agglomerates. The MSTO and MSTO-R lung cancer cells show greater cytosolic localization profiles for CAAKA (near 80 μm^2 or 84 ± 42 and 72 ± 18
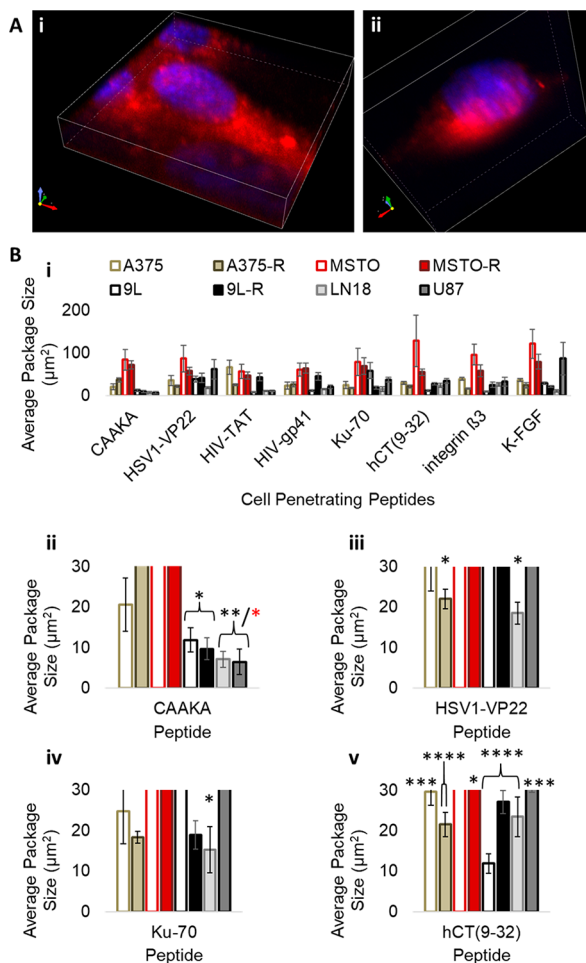
Figure 5. (A) Confocal fluorescent z-stack images of intracellular localization for QD-CPP constructs displaying more punctate endosomal fluorescence for QD-CAAKA (i) and more diffuse cytosolic localization for QD-hCT(9-32) (ii) in 9L cells. (B) Quantification of QD-CPP endosomal versus cytosolic localization by area of punctate fluorescence, showing mostly mixed endosomal (10 μm^2 single endosome) and cytosolic (900 μm^2 whole cell) localization for naïve and drug resistant human melanoma (A375 & A375-R), human mesothelioma (MSTO & MSTO-R), rat gliosarcoma (9L and 9L-R), and human glioblastoma (LN18 & U87), with (ii–v) endosomal area range for CAAKA versus the best performers: HSV1-VP22, Ku-70, and hCT(9-32), respectively. Displaying statistical differences of $p \leq 0.5$, 0.1, 0.001, and 0.0001 as *, **, ***, and ****, respectively, for fluorescence package sizes in comparison to MSTO cells (black) and drug resistant MSTO-R cells (red).

μm^2, respectively) as well as the best performers (~60–130 μm^2). This is in comparison to glioma cell lines which more distinctively show endosomal entrapment for the QD-CAAKA samples (near or below 10 μm^2), with HSV1-VP22, Ku-70, and hCT(9-32) each showing more cytosolic (average size greater than 30 μm^2) for one or more glioma cell lines (Figure 5Bii-iv). Statistical analysis of the averages fluorescence package sizes showed the greatest differences to be observed when compared to the MSTO cell line (which displays large fluorescence areas, likely indicating cytosolic diffusion), across the majority of CPPs (denoted by black asterisks in Figure 5Bii-iv), with the QD-hCT(9-32) experiencing the most meaningful differences between cell lines, with $p < 0.001$ for all but the MSTO-R line. A small statistical significance of $p <$

0.5 was also observed for MSTO-R, with regards to the QD-CAAKA (denoted by a red asterisk in Figure 5Bii). These results indicate that cellular processing profiles are likely more dependent on cell type than CPP.

Additional analysis of the percentage of punctate fluorescence relative to the total fluorescence area within each cell type is demonstrated in Supporting Information Figure SF4 and reveals that differences in punctate patterning had higher rates of statistical significance with the glioma cell lines of U87, LN18, and 9L/-R than did the melanoma (A375/-R) or mesothelioma (MSTO/-R) cell lines. However, differences within the glioma cell lines appear to be more CPP-dependent, with Ku-70 showing the highest punctate percentages in U87 and LN18, and HIV-TAT and HIV-gp41 showing the highest punctate percentages in 9L and 9L-R, respectively (Supporting Information Figure SF4).

These experimental observations are interesting findings as it has previously been assumed that nanoparticle delivery constructs disassemble during packaging in the endolysosomal pathway allowing escape of the cargo with only the NP being trafficked out of the cell via exocytosis.[54−57] Determination of the amount of cytosolic delivery versus endosomal escape in the cell, and what cellular uptake mechanisms may be involved with each of the cell penetrating peptides, will require future studies.

Computed CPP Orientation and Packing Analysis. Much of the recent literature suggests that cellular uptake of CPPs is highly dependent on electrostatic interactions of cell surface markers in addition to the positive charge of the peptide.[39] Although the set of peptides tested was not exhaustive, the data in Figures 3−5 suggest that uptake of the CPPs could rely more heavily on CPP interactions with cellular surface markers than previously anticipated. Most research indicates that CPPs gain access to the intracellular lumen through various endocytic pathways,[8] many of which require receptor mediated binding as an initiation step. Since acquisition of drug resistant status in cancer cell lines is known to cause a change in membrane composition and expression of different surface markers[58]−depending on the amount of resistance to the chemotherapeutics−these results may suggest that the ability and efficiency of CPP cellular uptake is not only sensitive to membrane surface markers available per cell type but also potentially to changes in the cellular membrane structure and prevalence or identity of surface receptors within tissue classes as well.

To further understand the peptide dependent uptake behavior, the nature of the potential packing and orientations of the appended peptides on the surface of the QD was analyzed using the PEP-FOLD structure predicting software service,[59] to assess the most energetically favorable structural conformations for the CPP sequences under physiological conditions. The generated results were further filtered to select the most plausible QD-bound secondary structure, which allowed for unhindered access of the thiol from the N-terminal cysteine to bind to the QD surface. In Figure 6 it can be seen that each peptide adopts a different degree of ordered secondary structure. These differences lead to unique structural morphologies which do not trend with the properties of the primary sequences; for instance, the peptides with higher numbers of amino acid residues in their sequences do not always display a proportionally greater height from the QD surface compared to shorter peptides in terms of sequence length (Table 3). Also, the folding orientations alter each
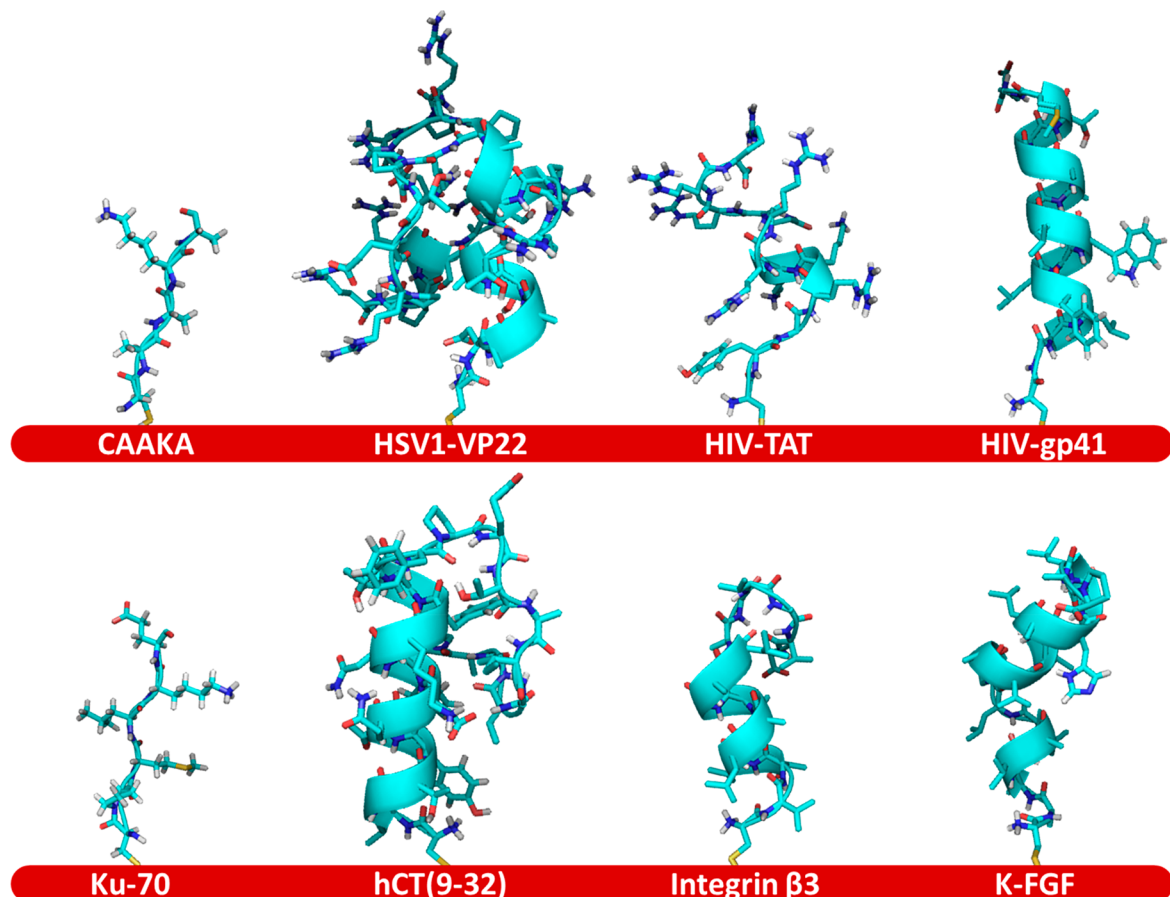
Figure 6. PEP-FOLD generated secondary structures of the studied CPPs as possible folding orientations of peptides bound to the QD surface via the N-terminal cysteine thiol.

Table 3. Calculated Peptide Properties and Loading Level on the 4 nm Diameter QD (surface area ~50 nm^2), Based on the PEP-FOLD Generated CPP Structures, Displaying Folded Peptide Height and Diameter Given in Angstroms (Å), Binding Footprint in Square Nanometers (nm^2), and the Maximum Number of Peptides that a 4 nm QD Could Accommodate for Single Peptide Loading (100%), and Ratioed Peptide Loading (90% & 10%) for CAAKA:CPPX.

CPP	Height (Å)	Diameter (Å)	Footprint (nm^2)	100% Loading (# per QD)	90% CAAKA (# per QD)	10% CPPX (# per QD)
CAAKA	15.1	9.0	0.6	79.0	--	--
HSV1-VP22	31.5	26.7	5.6	9.0	39.9	4.4
HIV-TAT	27.6	25.6	5.1	9.8	41.6	4.6
HIV-gp41	31.7	15.2	1.8	27.7	60.0	6.7
Ku-70	22.8	13.1	1.3	37.3	64.0	7.1
hCT(9-32)	28.1	16.6	2.2	23.2	57.3	6.4
Integrin β3	23.1	9.8	0.8	66.6	69.8	7.8
K-FGF	25.6	19.2	2.9	17.4	52.5	5.8

peptide's effective footprint, or the amount of "floorspace" that the peptide occupies on the QD surface, which impacts the CPP packing efficiency and loading level on the QDs (Table 3). Both the factors of CPP orientation and packing play an important role in the ability of the transduction sequences of the peptides to access and interact with the cellular membrane to promote cellular entry. The maximum possible numbers of peptides able to spatially fit on the QD surface (ignoring more complex steric or repulsive molecular interactions) can be seen in Table 3 for 100% loading and 10% loading versus CAAKA. Notably, the coloading of the short CAAKA filler sequence not only has the ability to aid in visibility of the longer target CPPs, giving up to an extra 16 Å calculated head clearance (depending on CPP), but may also aid in QD stability by

increasing the surface passivation and allowing for more binding sites on the QD to be occupied than if loaded with the target sequences alone (Table 3).

The calculations shown in Table 3 provide ideal packing ratios, and it is assumed that the actual CPP packing on the QD surface would be limited by the interactions of the coloaded CPPs. It is assumed that diversifying the loaded CPP properties, by coloading with the CAAKA peptide which has a positive charge on the lysine residue, may mitigate some tight packing affects caused by hydrophobic residue interactions near the QD surface. This may also result in increased flexibility and visibility of the CPPs to the cell surface by limiting close packing interactions of the peptides. Although the exact ratios of loaded peptides were not able to be

determined with the available analytical tools due to the similarities in peptide absorption and chemical shift profiles, the observation of differential uptake for each QD-CPP sample, versus the 100% CAAKA loaded QD (as a control complex), indicates that the target CPP sequences are able to impact cellular uptake when the constructs are assembled at a ratioed loading level of 1:9 CAAKA.

CONCLUSION

The selectivity of the various CPPs for drug-resistant cancer cell lines was analyzed and compared to the drug-naive cancer lines. The results of the study indicate that the uptake behavior is highly dependent on the cell type and its level of acquired resistance, as well as the CPP. The studied CPPs were selected from reported viral or signal protein sequences that have been demonstrated to cross cell membranes. The CPP sequences studies were modified with a N-terminal cysteine appended to truncated fragments of highly charged viral capsid proteins (HIV-TAT and HSV1-VP22)[31,34] and protein transduction domains with low charge (hCT(9-32), Ku-70, and K-FGF),[41,43,60] and neutral transduction sequences (HIV-gp41 and integrin-β3).[36,45] The CPPs coloaded onto the multi-shelled QDs at a 1:9 molar ratio versus the short synthetic peptide CAAKA. As indicated in the PEP-FOLD analysis (Figure 6) coloading increases the target CPP availability to the cell surface and potentially enhances recognition of the CPP sequence with the cell surface, by mitigating close packing of the CPP backbones around the QD delivery vector. The results indicate each CPP exhibits cell-specific uptake profiles with unique responses being observed for each cell line and peptide (Figures 3 and 4). Despite these cell-specific variations, significant uptake is observed for the hCT(9-32), Ku-70, and HSV1-VP22 peptides for the majority of the selected screen of cell lines, with significant increases being observed for the drug resistant human melanoma and rat gliosarcoma cells ($p < 0.05$ and 0.0001, respectively), which may be due to changes in membrane protein expression as cancer cells acquire drug resistance. Inspection of the sequences reveals the uptake profiles do not appear to be dependent on the peptide charge, length, or secondary structure; although peptide packing on the QD surface may affect cellular uptake. This work highlights the utility of multishelled QDs for effective CPP-mediated uptake screening in multiple cell lines using fluorescent microscopy, as well as demonstrates the nontrivial considerations involved in designing targeted nanotherapeutics for drug resistant cancer treatment.

This work demonstrates that, for the selected cells lines, differences in QD-CPP cellular uptake are dependent on the drug resistance status as well as the specific CPP used. Results from this study provide insight into the use of CPPs in cancer lines, as the CPPs can have variable transfection efficiency depending on cell type and drug resistance status of the cells. This is important for future endeavours in drug delivery designs, as targeting cancer *in vivo* does not have a "one-size-fits-all" solution, and different CPPs might be needed depending on the drug resistant status of the cells at the time of delivery. It is also observed that the QD does not cause toxicity and provides valuable insights into cell-specific uptake profiles. Future studies are needed to assess the effects of coappending a drug to the surface of the QD to determine the outcomes of a multibiofunctional multishelled QD-CPP, within these cell lines, in order to better understand the utility

of CPP conjugated nanoparticles as a viable therapeutic for drug delivery.

EXPERIMENTAL SECTION

Multishelled QD Synthesis. Spherical 4.3 nm multishelled CdTe@CdSe@CdS@ZnS quantum dots (QD) were prepared using a multistep step core—shell synthesis where the Cd stock solution (0.05 M) was prepared by dissolving CdO in tetradecyl phosphonic acid (0.125M) and octadecene (ODE) at 300°C under N_2. The 0.1 M Te stock solution was prepared by dissolving Te in trioctyl phosphine (TOP) and dilution by an equal volume of ODE. Similarly, 0.1 M solutions of TOP/ODE:Se, TOP/ODE:Cd(acetate), TOP/ODE:S, and TOP/ODE:ZDC (zinc diethyldithiocarbamate) were prepared as multishelling precursors. As a special note, the ZDC precursor decomposes at 70 °C, allowing it to act as both the zinc and sulfur source for the final ZnS shell. For this reason, care must be used during preparation and storage of the precursor, and the powder was dissolved by sonication in an ice bath.

The core CdTe was prepared by microwave heating of the Cd stock (4 mL, 0.05M) to 220 °C at 300 W under N_2, followed by rapid injection of the above-mentioned Te stock (2 mL, 0.1 M). The solution was maintained at 220 °C (300 W) for 2 min resulting in formation of the 3.4 nm CdTe core. Formation of a CdSe interface layer was accomplished in a stepwise SILAR approach, without isolation of the CdTe core by addition of 1 mL TOP/ODE:Se (0.1 M) at 150 °C (300 W) for 2 min, followed by precipitation using toluene and methanol, and centrifugation to isolate the CdTe@CdSe QD. The final two shell layers for the multilayer QD were added by dissolution of the CdTe@CdSe QD into ODE followed by heating to 150 °C in the MW cavity (300 W) and rapid injection of 0.1 M cadmium acetate in TOP/ODE followed by 0.1 M sulfur powder in TOP/ODE. The reaction was cooled to 135°C, and 0.1 M zinc diethyldithiocarbamate in TOP/ODE was added and allowed to react for 15 min with a final annealing step at 180°C for 15 min. The multishelled QD was isolated by precipitation through the addition of MeOH, washed three times by toluene/MeOH, and centrifuged to isolate a free-flowing powder.

The isolated QDs were analyzed by transmission electron microscopy (TEM) using a JEOL-2010 microscope operated at 200 kV. The samples were dispersed on 400 mesh holey carbon grids (Electron Microscopy Sciences) from a toluene solution. The core of the QD consisted of a ∼3.4 nm diameter CdTe nanosphere, with half monolayer of CdSe, one monolayer of CdS, and one monolayer of ZnS. The as-prepared QDs were passivated by trioctyl phosphine (TOP). The resulting multishelled QD had a 5% size dispersity based on TEM analysis. The first exciton for the QD was found to be at 606 nm with the band-edge emission observed at 665 nm (FWHM = 24 nm) with a QY of 33.7%.

Peptide Surface Passivation. Biphasic place exchange reactions were carried out to replace the organic soluble TOP passivating molecules with the hydrophilic peptides through formation of a bidentate coordination to the N-terminal cysteine of the CPPs. The purified N-terminal cysteine modified CPP sequences were purchased from RS Synthesis (Louisville, KY). The sequences are available in Table 1. The biphasic ligand exchange was accomplished using phase transfer from tetrachloroethylene (TCE) into water, by dissolution of the QD (5 mg, 2 μM) in 2 mL of TCE at 60 °C. A N_2 sparged, aqueous solution (2 mL) containing 2 M

peptide and 0.05 M TCEP was added to the TCE solution of QDs. The biphasic reaction was stirred at 60 °C for 10 min, followed by dropwise addition of 100 μL of tetraethylammonium hydroxide (20 wt %) in DI H_2O, every 10 min until the QDs were fully exchanged, typically within 1 h. Afterward, the reaction was allowed to phase separate and the water solubilized QD fraction was removed and stored at 4 °C. Prior to use, the CPP- QDs were isolated by two successive ethanol precipitations or by three successive solvent exchanges of 0.2 μM filtered H_2O using a 3k molecular weight cutoff spin filter (VWR) and resuspended in 0.2 μM filtered H_2O.

QD-CPP Characterization. QD-CPP constructs were assessed for optical properties using a Cary Bio-50 UV–vis spectrophotometer to determine any shift in the first exciton for each CPP preparation. Similarly, photoluminescent properties were assessed using a Varian Excite spectrophotofluorometer, with excitation at 580 nm. Quantum yields were calculated using Rhodamine 6G in ethanol (ϕ = 95%). QD-CPP zeta potentials were measured using a Wyatt Möbius in nanopore water in triplicate measurements of 10 scans collected over 10 s each. Relative QD-CPP size was also assessed using 0.7% agarose gel electrophoresis, at 80 V, 500 mA for 30 min at 25 °C. TEM images of peptide passivated QDs were also collected as described above, and analyzed for size distribution in ImageJ software.

Human Cell Lines and Culture. The human cancer cell lines used in this report were obtained from the American Type Culture Collection (ATCC). The human mesothelioma cell line MSTO-211H (CRL-2081) and the human malignant melanoma cell line A-375 (CRL-1619). A-375 skin cancer cells were acquired from ATCC and cultured at 37 °C and 5% CO_2 in RPMI 1640 medium (Sigma Chemical Co., St. Louis, MO) supplemented with 10% fetal bovine serum (Sigma) and penicillin/streptomycin (Gibco). Drug resistant cell lines were established as described previously.[61] Additionally, human drug resistant glioblastoma lines U-87 MG (ATCC HTB-14) and LN-18 (ATCC CRL-2610) were acquired and cultured at 37 °C and 5% CO_2 in Dubelco's Modified Eagles Medium (DMEM 7777, Sigma), with 10% FBS (Sigma), penicillin/streptomycin/amphotericin B (Sigma), and gentamicin (Gibco).

Rat Gliosarcoma Cell Lines and Culture. Rat gliosarcoma cells (9L) were acquired from the neurotissue bank at the University of California, San Francisco. Subcultures of 9L cells were expanded in 75 cm^2 plastic flasks (T-75 cm^2, Nunc) with DMEM (D7777 Sigma Chemical Co., St Louis, MO), supplemented with 2 mM L-glutamine, 100 μg/mL gentamicin, 0.1% pen/strep, and 10% fetal bovine serum (HyClone) generating DMEM complete medium. The cultures were incubated at 37 °C in a humidified atmosphere containing 5% CO_2. The 9L cells were split into 4 identical flasks. Control, BCNU-sensitive 9L cells (9L) were grown as described above. BCNU-resistant 9L cells (9L-R) were created by challenging 9L cells with increasing concentrations of BCNU (10−225 μM) over time. Surviving cells were grown to confluence and then split into new flasks, allowed to reach 80% confluence, and treated again with complete media or complete media containing BCNU.

Responsiveness of 9L and 9L-R subcultures to chemotherapeutics was determined using the *In Vitro* Toxicology Assay Kit (Sigma-Aldrich TOX-6) based on the sulforhodamine blue (SRB) method for monitoring cell viability. Briefly, cells were plated in 96-well plates, in triplicate, at a density of 1

× 10^5 cells/mL and treated for 72 h using the range of indicated concentrations of drugs. After 72 h, cells were fixed by adding 50 μL of ice cold 50% trichloroacetic acid (TCA) per well for 1 h at 4 °C. After washing, plates were air-dried before addition of 100 μL of 0.4% sulforhodamine blue. The plates were then washed with 1% acetic acid and air-dried. The incorporated dye was solubilized by the addition of 200 μL of 10 mM Tris buffer per well. Absorbance was read on a BioRad Benchmark Microplate reader at 490−530 nm to characterize protein concentration in each well.

Cellular Uptake Studies and Fluorescent Microscopy. For each cancer cell line, cells were plated at 30% confluence (~30,000 cells/cm^2) on 1.0 coverglass in 24-well plates (Corning) and grown for 24 h at 37 °C in 5% CO_2 prior to transfection with 2 pmol of QD-CPP per well (1 nM). After 24 h incubation with the QD-CPPs at 37 °C in 5% CO_2, the media was removed and the cells were rinsed with prewarmed PBS, fixed with 4% paraformaldehyde (PFA) (Sigma), stained with DAPI nuclear stain (Life Technologies), and mounted to slides with Fluorogel antifade mounting media (Electron Microscopy Sciences), according to the manufacturers' instructions. Fixed slides were stored at 4°C in the dark when not under microscopic observation.

Cellular uptake was analyzed under fluorescent microscopy using a Nikon Eclipse TE2000 inverted microscope. Excitation of QD-CPPs was performed using the Texas Red filter cube (Nikon) with a 500 ms exposure time. The DAPI nuclear stain was used to correct QD fluorescence per cell number and was excited with a DAPI filter cube (Nikon) for 300 ms of exposure. Differential interference contrast (DIC) images were collected to visualize the cell boundaries, with 35 ms of light exposure.

Image Analysis. All images were analyzed in ImageJ software[62] for the total QD fluorescence intensity corrected for cell number and quantum yield differences between QD-CPPs, as observed during photoluminescence characterization in a cuvette. Analysis of cellular localization of the QD-CPPs was performed in ImageJ by assessing intensity-thresholded images for the average fluorescence package 2-dimentional area, with N = 9 images per QD-CPP sample per cell line, and approximately 500−2500 packages measured per image. Statistical analysis was performed using a two-way ANOVA with Tukey's post hoc test in GraphPad software (Prism). Lower limit thresholds were set to just above the noise floor in order to calculate the total fluorescence area. For punctate fluorescence calculations, the lower limit thresholds were set to 100 counts, in order to eliminate dilute cytosolic fluorescence contributions. Calculated punctate versus total fluorescence values were used to determine calculated punctate fluorescence percentages.

■ ASSOCIATED CONTENT

Ⓢ Supporting Information

The Supporting Information is available free of charge on the ACS Publications website at DOI: 10.1021/acs.bioconj-chem.8b00429.

> QD characterization data, gel electrophoresis, and optical image analysis (PDF)

■ AUTHOR INFORMATION

Corresponding Author
*E-mail: strouse@chem.fsu.edu.

ORCID
Kate J. F. Carnevale: 0000-0001-6898-0381
Diego A. R. Zorio: 0000-0003-1761-7878
Geoffrey F. Strouse: 0000-0003-0841-282X

Present Addresses
§(M.E.M.) Navy Research Laboratory, Washington, DC, 20375.
‖(M.E.F.) University of North Georgia, Dahlonega, GA 30597.
⊥(G.L.) University of Wellington, Wellington, New Zealand.
#(R.K.) Andrew College, Cuthbert, GA 39840.

Notes
The authors declare no competing financial interest.

■ ABBREVIATIONS
QD, quantum dot; CPP, cell penetrating peptide; MDR, multidrug resistance

■ REFERENCES
(1) Chugh, A., Eudes, F., and Shim, Y. S. (2010) Cell-penetrating peptides: Nanocarrier for macromolecule delivery in living cells. *IUBMB Life 62*, 183−193.

(2) Margus, H., Padari, K., and Pooga, M. (2012) Cell-penetrating peptides as versatile vehicles for oligonucleotide delivery. *Mol. Ther. 20*, 525−533.

(3) Moschos, S. A., Jones, S. W., Perry, M. M., Williams, A. E., Erjefalt, J. S., Turner, J. J., Barnes, P. J., Sproat, B. S., Gait, M. J., and Lindsay, M. A. (2007) Lung delivery studies using siRNA conjugated to TAT(48−60) and penetratin reveal peptide induced reduction in gene expression and induction of innate immunity. *Bioconjugate Chem. 18*, 1450−1459.

(4) Rahmat, D., Khan, M. I., Shahnaz, G., Sakloetsakun, D., Perera, G., and Bernkop-Schnurch, A. (2012) Synergistic effects of conjugating cell penetrating peptides and thiomers on non-viral transfection efficiency. *Biomaterials 33*, 2321−2326.

(5) Lee, J. Y., Choi, Y. S., Suh, J. S., Kwon, Y. M., Yang, V. C., Lee, S. J., Chung, C. P., and Park, Y. J. (2011) Cell-penetrating chitosan/doxorubicin/TAT conjugates for efficient cancer therapy. *Int. J. Cancer 128*, 2470−2480.

(6) Muroski, M. E., Carnevale, K. J. F., Riskowski, R. A., and Strouse, G. F. (2015) Plasmid transfection in mammalian cells spatiotemporally tracked by a gold nanoparticle. *ACS Nano 9*, 124−133.

(7) Gupta, A., Moyano, D. F., Parnsubsakul, A., Papadopoulos, A., Wang, L. S., Landis, R. F., Das, R., and Rotello, V. M. (2016) Ultrastable and Biofunctionalizable Gold Nanoparticles. *ACS Appl. Mater. Interfaces 8*, 14096−14101.

(8) Mueller, J., Kretzschmar, I., Volkmer, R., and Boisguerin, P. (2008) Comparison of cellular uptake using 22 CPPs in 4 different cell lines. *Bioconjugate Chem. 19*, 2363−2374.

(9) Chen, B., Liu, Q., Zhang, Y., Xu, L., and Fang, X. (2008) Transmembrane delivery of the cell-penetrating peptide conjugated semiconductor quantum dots. *Langmuir 24*, 11866−11871.

(10) Fonseca, S. B., Pereira, M. P., and Kelley, S. O. (2009) Recent advances in the use of cell-penetrating peptides for medical and biological applications. *Adv. Drug Delivery Rev. 61*, 953−964.

(11) Chen, N. T., Cheng, S. H., Liu, C. P., Souris, J. S., Chen, C. T., Mou, C. Y., and Lo, L. W. (2012) Recent Advances in Nanoparticle-Based Forster Resonance Energy Transfer for Biosensing, Molecular Imaging and Drug Release Profiling. *Int. J. Mol. Sci. 13*, 16598−16623.

(12) Ezzat, K., Zaghloul, E. M., El Andaloussi, S., Lehto, T., El-Sayed, R., Magdy, T., Smith, C. I., and Langel, U. (2012) Solid formulation of cell-penetrating peptide nanocomplexes with siRNA and their stability in simulated gastric conditions. *J. Controlled Release 162*, 1−8.

(13) Copolovici, D. M., Langel, K., Eriste, E., and Langel, Ü. (2014) Cell-penetrating peptides: Design, synthesis, and applications, *ACS Nano 8*, 1972−1994.

(14) Siegel, R. L., Miller, K. D., and Jemal, A. (2016) Cancer statistics, 2016. *Ca-Cancer J. Clin. 66*, 7−30.

(15) Ma, X., Yafeng, L., Jia, L., Donghai, W., Qibing, H., Xinyu, W., Gang, L., Shujun, X., and Xingang, L. (2009) Survival analysis of 205 patients with glioblastoma multiforme: clinical characteristics, treatment and prognosis in China. *J. Clin. Neurosci. 16*, 1595−1598.

(16) Pichlmeier, U., Andrea, B., Gabriele, S., and Walter, S. (2008) Resection and survival in glioblastoma multiforme: an RTOG recursive partitioning analysis of ALA study patients. *Neuro. Oncol. 10*, 1025−1034.

(17) Mellor, H. R., and Callaghan, R. (2008) Resistance to Chemotherapy in Cancer: A Complex and Integrated Cellular Response. *Pharmacology 81*, 275−300.

(18) Rebucci, M., and Michiels, C. (2013) Molecular aspects of cancer cell resistance to chemotherapy. *Biochem. Pharmacol. 85*, 1219−1226.

(19) Farrell, A. (2011) A close look at cancer. *Nat. Med. 17*, 262−265.

(20) Bondy, M. L., Scheurer, M. E., Malmer, B., and Barnholtz-Sloan, J. S. (2008) Brain tumor epidemiology: consensus from the Brain Tumor Epidemiology Consortium. *Cancer 113*, 1953−1968.

(21) Fisher, J., Schwartzbaum, J., Wrensch, M., and Wiemels, J. L. (2007) Epidemiology of Brain Tumors. *Neurol. Clincs 25*, 867−890.

(22) Liu, B. R., Huang, Y. W., Chiang, H. J., and Lee, H. J. (2010) Cell-penetrating peptide-functionalized quantum dots for intracellular delivery. *J. Nanosci. Nanotechnol. 10*, 7897−7905.

(23) Cheng, Y., Dai, Q., Morshed, R. A., Fan, X., Wegscheid, M. L., Wainwright, D. A., Han, Y. Y., Zhang, L., Auffinger, B., Tobias, A. L., et al. (2014) Blood-Brain Barrier Permeable Gold Nanoparticles: An Efficient Delivery Platform for Enhanced Malignant Glioma Therapy and Imaging. *Small 10*, 5137−5150.

(24) Muroski, M. E., Morgan, T. J. T. J., Levenson, C. W., and Strouse, G. F. (2014) A Gold Nanoparticle Pentapeptide: Gene Fusion To Induce Therapeutic Gene Expression in Mesenchymal Stem Cells. *J. Am. Chem. Soc. 136*, 14763−14771.

(25) Zhang, W. J., Chen, G. J., Wang, J., Ye, B. C., and Zhong, X. H. (2009) Design and synthesis of highly luminescent near-infrared-emitting water-soluble CdTe/CdSe/ZnS Core/Shell/Shell quantum dots. *Inorg. Chem. 48*, 9723−9731.

(26) Keller, A. A., Mussbach, F., Breitling, R., Hemmerich, P., Schaefer, B., Lorkowski, S., and Reissmann, S. (2013) Relationships between cargo, cell penetrating peptides and cell type for uptake of non-covalent complexes into live cells. *Pharmaceuticals 6*, 184−203.

(27) Jobin, M. L., Blanchet, M., Henry, S., Chaignepain, S., Manigand, C., Castano, S., Lecomte, S., Burlina, F., Sagan, S., and Alves, I. D. (2015) The role of tryptophans on the cellular uptake and membrane interaction of arginine-rich cell penetrating peptides. *Biochim. Biophys. Acta, Biomembr. 1848*, 593−602.

(28) Milletti, F. (2012) Cell-penetrating peptides: classes, origin, and current landscape. *Drug Discovery Today 17*, 850−860.

(29) Normand, N., van Leeuwen, H., and O'Hare, P. (2001) Particle formation by a conserved domain of the herpes simplex virus protein VP22 facilitating protein and nucleic acid delivery. *J. Biol. Chem. 276*, 15042−50.

(30) Zender, L., Kühnel, F., Köck, R., Manns, M., and Kubicka, S. (2002) VP22-mediated intercellular transport of p53 in hepatoma cells in vitro and in vivo. *Cancer Gene Ther. 9*, 489−96.

(31) Elliott, G., and O'Hare, P. (1997) Intercellular trafficking and protein delivery by a herpesvirus structural protein. *Cell 88*, 223−233.

(32) Frankel, A. D., and Pabo, C. O. (1988) Cellular uptake of the tat protein from human immunodeficiency virus. *Cell 55*, 1189−1193.

(33) Murakami, T., and Freed, E. O. (2000) The long cytoplasmic tail of gp41 is required in a cell type-dependent manner for HIV-1

envelope glycoprotein incorporation into virions. *Proc. Natl. Acad. Sci. U. S. A. 97*, 343−8.

(34) Green, M., and Loewenstein, P. M. (1988) Autonomous functional domains of chemically synthesized human immunodeficiency virus tat trans-activator protein. *Cell 55*, 1179−1188.

(35) Vives, E., Brodin, P., and Lebleu, B. (1997) A truncated HIV-1 Tat protein basic domain rapidly translocates through the plasma membrane and accumulates in the cell nucleus. *J. Biol. Chem. 272*, 16010−16017.

(36) Morris, M. C., Vidal, P., Chaloin, L., Heotz, F., and Divita, G. (1997) A new peptide vector for efficient delivery of oligonucleotide into nontransformed mammalian cells. *Nucleic Acid Res. 25*, 2730−2736.

(37) Koren, E., and Torchilin, V. P. (2012) Cell-penetrating peptides: breaking through to the other side. *Trends Mol. Med. 18*, 385−393.

(38) Wybranietz, W. A., Prinz, F., Spiegel, M., Schenk, A., Bitzer, M., Gregor, M., and Lauer, U. M. (1999) Quantification of VP22-GFP spread by direct fluorescence in 15 commonly used cell lines. *J. Gene Med. 1*, 265−274.

(39) Falanga, A., Galdiero, M., and Galdiero, S. (2015) Membranotropic Cell Penetrating Peptides: The Outstanding Journey. *Int. J. Mol. Sci. 16*, 25323−25337.

(40) Walker, J. R., Corpina, R. A., and Goldberg, J. (2001) Structure of the Ku heterodimer bound to DNA and its implications for double-strand break repair. *Nature 412*, 607−614.

(41) Gomez, J. A., Gama, V., Yoshida, T., Sun, W., Hayes, P., Leskov, K., Boothman, D., and Matsuyama, S. (2007) Bax-inhibiting peptides derived from Ku70 and cell-penetrating pentapeptides. *Biochem. Soc. Trans. 35*, 797−801.

(42) Krauss, U., Kratz, F., and Beck-Sickinger, A. G. (2003) Novel daunorubicin-carrier peptide conjugates derived from human calcitonin segments. *J. Mol. Recognit. 16*, 280−287.

(43) Machova, Z., Muhle, C., Krauss, U., Trehin, R., Koch, A., Merkle, H. P., and Beck-Sickinger, A. G. (2002) Cellular internalization of enhanced green fluorescent protein ligated to a human calcitonin-based carrier peptide. *ChemBioChem 3*, 672−677.

(44) Wagner, K., Van Mau, N., Boichot, S., Kajava, A. V., Krauss, U., Le Grimellec, C., Beck-Sickinger, A., and Heitz, F. (2004) Interactions of the human calcitonin fragment 9−32 with phospholipids: a monolayer study. *Biophys. J. 87*, 386−395.

(45) Liu, X. Y., Timmons, S., Lin, Y. Z., and Hawiger, J. (1996) Identification of a functionally important sequence in the cytoplasmic tail of integrin beta 3 by using cell-permeable peptide analogs. *Proc. Natl. Acad. Sci. U. S. A. 93*, 11819−24.

(46) Bovi, P. D., Curatola, A. M., Kern, F. G., Greco, A., Ittmann, M., and Basilico, C. (1987) An oncogene isolated by transfection of Kaposi's sarcoma DNA encodes a growth factor that is a member of the FGF family. *Cell 50*, 729−737.

(47) Ray, P. E., Al-Attar, A., Liu, X. H., Das, J. R., Tassi, E., and Wellstein, A. (2014) Expression of a secreted fibroblast growth factor binding protein-1 (FGFBP1) in Angioproliferative Kaposi Sarcoma. *J. AIDS Clin. Res. 5*, 309.

(48) Yang, N. J., and Hinner, M. J. (2015) Getting across the cell membrane: an overview for small molecules, peptides, and proteins. *Methods Mol. Biol. 1266*, 29−53.

(49) Chakrabarti, A. C. (1994) Permeability of membranes to amino acids and modified amino acids: mechanisms involved in translocation. *Amino Acids 6*, 213−29.

(50) Sawada, M., Hayes, P., and Matsuyama, S. (2003) Cytoprotective membrane-permeable peptides designed from the Bax-binding domain of Ku70. *Nat. Cell Biol. 5*, 352−357.

(51) Marks, J. R., Placone, J., Hristova, K., and Wimley, W. C. (2011) Spontaneous membrane-translocating peptides by orthogonal high-throughput screening. *J. Am. Chem. Soc. 133*, 8995−9004.

(52) Pons, T., Uyeda, H. T., Medintz, I. L., and Mattoussi, H. (2006) Hydrodynamic dimensions, electrophoretic mobility, and stability of hydrophilic quantum dots. *J. Phys. Chem. B 110*, 20308−20316.

(53) Freitas, C., and Müller, R. H. (1998) Effect of light and temperature on zeta potential and physical stability in solid lipid nanoparticle (SLN®) dispersions. *Int. J. Pharm. 168*, 221−229.

(54) Chithrani, B. D., and Chan, W. C. W. (2007) Elucidating the mechanism of cellular uptake and removal of protein-coated gold nanoparticles of different sizes and shapes. *Nano Lett. 7*, 1542−1550.

(55) Oh, N., and Park, J. H. (2014) Surface chemistry of gold nanoparticles mediates their exocytosis in macrophages. *ACS Nano 8*, 6232−6241.

(56) Dombu, C. Y., Kroubi, M., Zibouche, R., Matran, R., and Betbeder, D. (2010) Characterization of endocytosis and exocytosis of cationic nanoparticles in airway epithelium cells. *Nanotechnology 21*, 355102.

(57) Jiang, X., Röcker, C., Hafner, M., Brandholt, S., Dörlich, R. M., and Nienhaus, G. U. (2010) Endo- and Exocytosis of Zwitterionic Quantum Dot Nanoparticles by Live HeLa Cells. *ACS Nano 4*, 6787−6797.

(58) Lavie, Y., and Liscovitch, M. (2000) Changes in lipid and protein constituents of rafts and caveolae in multidrug resistant cancer cells and their functional consequences. *Glycoconjugate J. 17*, 253−259.

(59) Shen, Y., Maupetit, J., Derreumaux, P., and Tufféry, P. (2014) Improved PEP-FOLD approach for peptide and miniprotein structure prediction. *J. Chem. Theory Comput. 10*, 4745−4758.

(60) Manceur, A., Wu, A., and Audet, J. (2007) Flow cytometric screening of cell-penetrating peptides for their uptake into embryonic and adult stem cells. *Anal. Biochem. 364*, 51−59.

(61) Kenworthy, R., Bosco, D. B., DeLigio, J. T., and Zorio, D. A. R. (2018) Micro-RNA149 confers taxane resistance to malignant mesothelioma cells via regulation of P-glycoprotein expression. *Cancer Biol. Ther. 19*, 181−187.

(62) Schindelin, J., Arganda-Carreras, I., Frise, E., Kaynig, V., Longair, M., Pietzsch, T., Preibisch, S., Rueden, C., Saalfeld, S., Schmid, B., et al. (2012) Fiji: an open-source platform for biological-image analysis. *Nat. Methods 9*, 676−682.